Mechanism for embedded in-plane self-assembled nanowire formation

Nathaniel S. Wilson,[1] Stephan Kraemer,[2] Daniel J. Pennachio,[1] Patrick Callahan,[1]
Mihir Pendharkar,[3] and Christopher J. Palmstrøm[1,3,*]
[1]*Department of Materials, University of California, Santa Barbara, California 93106-5050, USA*
[2]*Center for Nanoscale Systems, Harvard University, Boston, Massachusetts 02138, USA*
[3]*Department of Electrical and Computer Engineering, University of California, Santa Barbara, California 93106-5050, USA*

(Received 31 July 2019; revised manuscript received 24 February 2020; accepted 27 February 2020;
published 17 June 2020)

We report a growth mechanism that produces in-plane $[1\bar{1}0]$ oriented ErSb nanowires formed during codeposition of $Er_{0.3}Ga_{0.7}Sb$ via molecular beam epitaxy (MBE). Nanowires are characterized by *in situ* scanning tunneling microscopy (STM), as well as *ex situ* transmission electron microscopy (TEM) and electron channeling contrast imaging. We show that complexes of macrosteps with step heights on the order of 7 nm form during nanowire growth. The macrosteps are shown to be part of the in-plane nanowire growth process and are directly responsible for the observed stratified distribution of in-plane nanowires. TEM indicates that initial growth results in out-of-plane nanowires transitioning to in-plane nanowires after a critical film thickness. A surface energy model is put forward that shows the critical thickness is due to minimization of the GaSb{110} surfaces formed during out-of-plane nanowire growth. Kinetics of the transition are discussed with respect to observed features in STM, along with the material parameters needed to achieve in-plane nanowire growth.

DOI: 10.1103/PhysRevMaterials.4.066003

I. INTRODUCTION

Spontaneous phase separation resulting in self-assembled nanostructures has been observed in a wide range of materials systems including semiconductors [1], oxides [2], and metals [3]. Often these nanostructures show desirable properties resulting from orientation [4], confinement [5], or increased coupling with a matrix material [1], making them an exciting area of interest when looking for new material properties. Spinodal decomposition and the resulting microstructures have long been an area of interest in bulk materials [6] but the behavior is less well understood during thin film growth processes such as molecular beam epitaxy (MBE). The role of strain in phase separation during MBE growth has been the subject of many studies [7,8] but the self-assembly of nanostructures in film growth is further complicated by surface specific kinetics and effects. Understanding the processes governing spontaneous phase separation in a surface dominated regime like MBE growth is imperative to enable engineering of self-assembled nanostructures during thin film growth.

The rare-earth/monopnictide (RE-V)–III-V compound semiconductor material system is an ideal test bed for investigating nanostructures formed by spontaneous phase separation. Most RE-Vs compounds have the rocksalt (NaCl) crystal structure and are typically semimetals that were initially studied for use as thermodynamically stable epitaxial contacts to III-V semiconductors [9–14]. Epitaxial growth of RE-V on III-V is relatively easily achieved due to similar lattice constants and a continuous group V atomic lattice between both crystal structures. However, one of the primary challenges for this material is defect formation during overgrowth of III-V's on RE-V due to the difference in the surface symmetry and bonding of the III-V (001) and the RE-V (001) surfaces. They are twofold and covalent and fourfold and ionic for the III-V and RE-V, respectively [15]. Hence, most III-V overgrowth efforts have moved away from complete RE-V thin film coverage to structures with embedded RE-V nanoparticles in a III-V matrix [16,17]. This allows for seeding on a III-V surface and lateral overgrowth over the RE-V, and shows particular promise with the use of surfactants [18,19]. The majority of current research in this area focuses on the ErAs material system where ErAs nanoparticles in a GaAs or InGaAs matrix have found use in a number of applications, such as photomixers [20], tunnel junctions [21], thermoelectrics [3,22], and may be used to influence quantum dot formation [23]. Interest has also recently expanded to similar materials such as TbAs and LuAs, which may form semiconducting nanoparticles [24], and TbAs/ErAs core-shell nanostructures [25]. All of these applications take advantage of the fact that RE-V materials are well suited to nanoparticle nucleation due to the low solid solubility of rare earths within III-V semiconductors as well as RE-V stability, resistance to diffusion, compatible crystal structures, and lattice matching [11,26,27].

The ErSb/GaSb material system studied in this work has exhibited the widest range of different nanostructures seen in a RE-V/III-V material system including isotropic nanoparticles, vertical nanowires, horizontal nanowires, and nanosheets, all of which are accessible by controlling the Er to Ga flux ratio [28]. The formation of nanoparticles and vertical nanowires is explained by an embedded growth mode where Er adatoms replace Ga in the first 3-4 monolayers of the GaSb surface [28–30]. ErSb's lower heat of formation is the driving force

---

[*] Corresponding author: cpalmstrom@ece.ucsb.edu

behind embedded growth and, combined with the difference in surface energies, which discourages GaSb growth on ErSb, results in vertical nanowires [29]. However, this model fails to provide a mechanism for the formation of the stratified layers of horizontal nanowires and nanosheets observed at Er concentrations in excess of 30%. It is important to understand the formation mechanism behind these structures if they are to be incorporated into sensitive device heterostructures and an in-depth understanding of the formation mechanism for these nanostructures may enable identification and engineering of other material systems with similar behavior.

II. EXPERIMENTAL PROCEDURE

Samples were grown in an arsenic and antimony containing III-V VG-V80H molecular beam epitaxy (MBE) chamber with a background pressure of $< 5\times10^{-11}$ Torr. The substrate temperature was measured by an optical pyrometer, calibrated to 540 °C at the GaSb(001) substrate oxide desorption temperature as observed by reflection high energy electron diffraction. Each sample was grown with a buffer layer of 100–250 nm of GaSb doped with Be at 5×10^{18} cm^{-3} at a substrate temperature of 480 °C to ensure a smooth surface before nanowire growth began. For nanowire growth, the substrate temperature was increased to 530 °C so that GaSb growth was in a step flow regime [31]. Nanowires were grown by codeposition of Er and Ga from elemental sources along with an overpressure of Sb$_2$ provided by an antimony valved cracker effusion cell. The nanostructures were initially characterized *in situ* by scanning tunneling microscopy (STM), imaging the growth surface without oxidation or contamination. The STM measurements were performed in an Omicron Low Temperature STM at 77 K with a tungsten tip and a tunneling current of 30 pA. Tip bias varied from -2V to 2V depending if the surface was primarily GaSb or ErSb. Scanning tunneling spectroscopy (STS) was performed using a variable tip height method by applying an additional AC voltage on the STM tip and measuring the resulting AC signal with a lock-in amplifier. STS data was processed and normalized to approximate local density of states in the manner described by Feenstra [32].

III. RESULTS

Prior to growth of nanowires by codeposition an embedded growth mode was confirmed by depositing 0.15 monolayers of Er on a GaSb surface, Fig. 1(a). Embedded nucleation is observed, ErSb has only 3.7% surface coverage instead of 15%, consistent with four-monolayer-thick nanostructures. The ErSb nanostructures protrude one monolayer out of the GaSb surface implying three monolayers are embedded in the GaSb matrix, in agreement with the previously observed embedded growth mode [28]. Figure 1(b) shows typical STS spectra of the sample where a metallic density of states is observed at the ErSb nanoparticles, while the GaSb matrix shows a gapped semiconducting density of states. Identification of surface reconstructions on later samples was performed by comparing STS to the ErSb and GaSb results from this known surface.

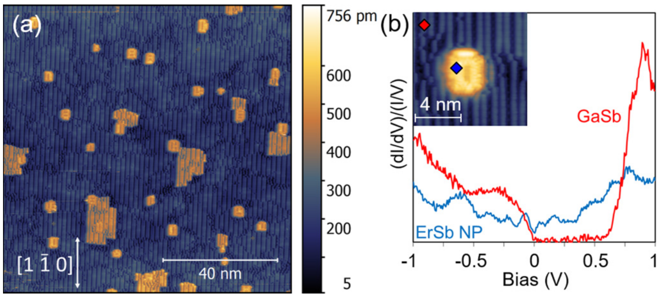

FIG. 1. (a) STM of 0.15 monolayers of ErSb deposited on GaSb(001) surface, -0.3V bias. (b) STS of ErSb nanoparticle where GaSb (red) shows a clear gap in its density of states, and ErSb (blue) appears metallic.

A. Surface morphology

Previous work has shown that codeposited Er$_x$Ga$_{1-x}$Sb with Er concentrations of $X = 0.1-0.25$ results in ErSb nanowires oriented out-of-plane [28]. These nanowires grow as ErSb preferentially deposits on previously nucleated ErSb particles [28]. As additional Er and Ga is deposited the nanoparticles elongate in the out-of-plane direction and are typically observed in small pits in the GaSb matrix [28]. At higher Er concentrations in-plane nanowires are observed. In-plane nanowire structures have nanowires rotated 90° from the out-of-plane configuration and are all oriented to extend along the [1$\bar{1}$0]. Evidence in this manuscript will show that large GaSb macrosteps several nanometers in height also form during in-plane nanowire growth. To aid in understanding these complex nanostructures Fig. 2 schematically shows the orientation of nanowires and GaSb macrosteps observed for in-plane and out-of-plane nanowire growth using both a top down view of the (001) growth surface, and a cross-sectional view of a cut exposing the (110) plane.

Figure 3 displays STM topography images of Er$_x$Ga$_{1-x}$Sb films grown with compositions of $X = 0.2, 0.25, 0.3$. The

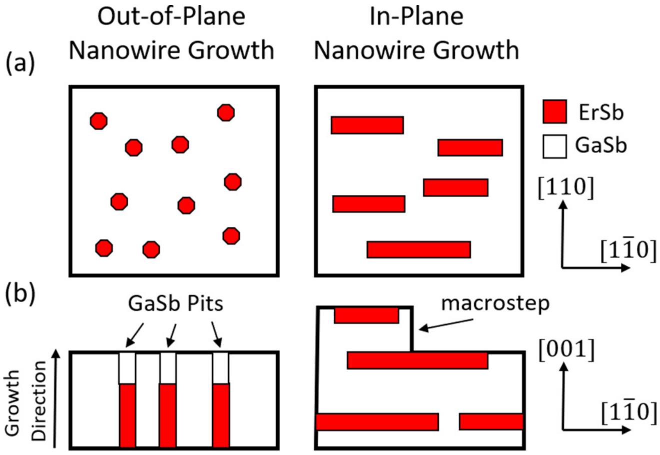

FIG. 2. Diagram of ErSb nanostructures (a) looking down on the (001) growth surface of an Er$_x$Ga$_{x-1}$Sb sample and (b) a cross-sectional schematic looking along the [110] direction. Images on the left side show schematically what happens during out-of-plane nanowire growth when $x < 0.3$ and images on the right show in-plane nanowire growth occurring when $x > 0.3$.

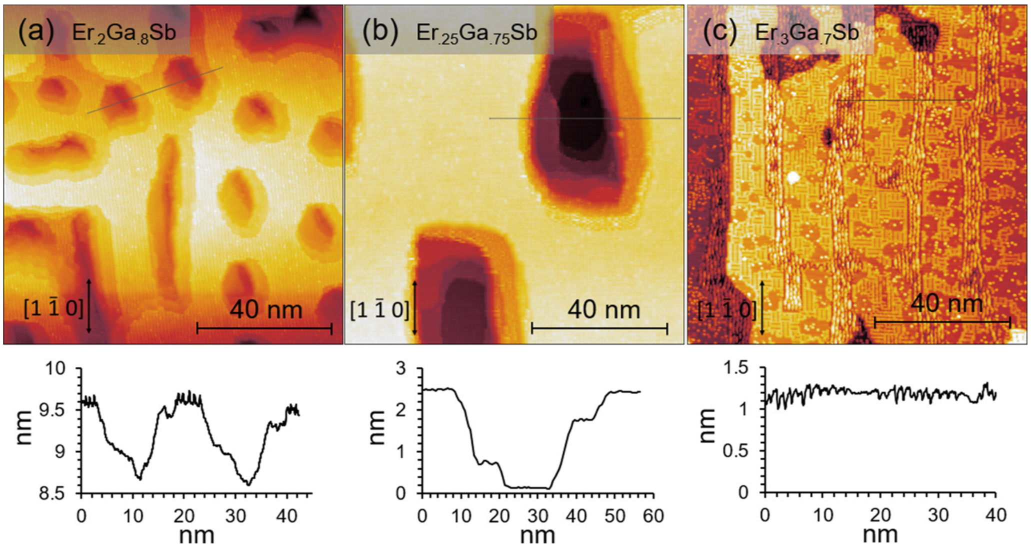

FIG. 3. STM and line scan of (a) $Er_{0.2}Ga_{0.8}Sb(001)$ surface with ErSb particles at base of pits, (b) $Er_{0.25}Ga_{0.75}Sb(001)$ surface with ErSb particles at base of pits and (c) $Er_{0.3}Ga_{0.7}Sb(001)$ surface where ErSb nanowires lie in the surface plane. Line scans in each case are across an ErSb nanoparticle.

$Er_{0.2}Ga_{0.8}Sb$ surface has a GaSb surface populated with several pits, this closely matches the surface previously observed for out-of-plane nanowire growth, which shows out-of-plane ErSb nanowires at the bottom of pits in the GaSb matrix [28]. As the Er content is increased to $Er_{0.25}Ga_{0.75}Sb$ vertical nanowires are still observed although the pits are noticeably larger and deeper. At $Er_{0.3}Ga_{0.7}Sb$ two changes in the surface morphology are observed. The first is that the transition to in-plane nanowires has occurred and pits around the nanowires have disappeared. On this surface ErSb nanowires lie in plane with the GaSb(001) surface and are elongated along the $[1\bar{1}0]$ see Fig. 3(c). ErSb nanoparticles sticking more than one monolayer out of the surrounding GaSb matrix are not observed suggesting that embedded growth of ErSb may occur at nanoparticle edges. The elongation of nanoparticles into wires along the $[1\bar{1}0]$ is likely due to asymmetric diffusion rates of the c(2×6) reconstructed GaSb(001) surface where an easy diffusion direction down the dimer rows along the $[1\bar{1}0]$ exists, a feature seen on similar surface reconstructions in GaAs [29,33].

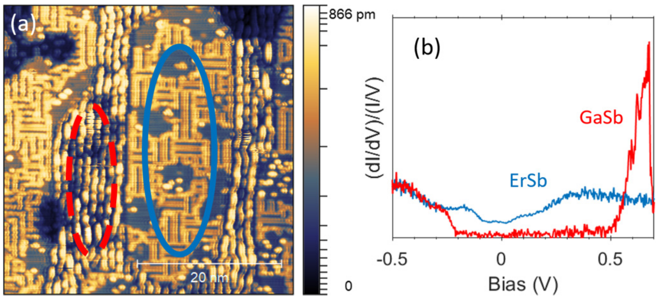

FIG. 4. (a) A section of the same STS topographic map shown in Fig. 3(c), a nonlinear height scale is used to accentuate the surface reconstructions. Dashed red circle indicates a region of GaSb surface probed by STS, the solid blue circle indicates an ErSb nanowire probed by STS. (b) STS spectra of the two regions highlighted in 4(a), the ErSb spectra is metallic and the GaSb spectra has a bandgap of 0.7 eV. The GaSb spectra is scaled down by a factor of 3 to aid in comparison.

The position and orientation of the in-plane nanowires can be observed from surface reconstructions of the growth surface. Figure 4 is an STM image with nonlinear height scale to accentuate the two observed surface reconstructions with paired STS spectra. The region in the solid blue oval has a "crosshatched" reconstruction that appears sporadically on the surface. This is consistent with reconstructions observed previously for 10 monolayer ErSb thin films [29]. STS data taken from within the solid blue oval confirms a metallic density of states as observed for the ErSb nanoparticles in Fig. 1. The dashed red oval corresponds to the $c(2\times6)$ GaSb surface reconstruction. STS from within the dashed red oval confirms a density of states with a band gap of ~0.7 eV in agreement with the bandgap of GaSb and the spectra observed for GaSb in Fig. 1. The dimers of the $c(2\times6)$ reconstruction are ordered over a longer distance in Fig. 1 thus the reconstruction within the red oval of Fig. 4 appears slightly wavy in comparison, this difference is prescribed to slight differences in Sb overpressure and the exact timing of removing the Sb flux while cooling the sample down from growth temperature.

The second change in the surface morphology is that large macrosteps are now present when reaching a composition of $Er_{0.3}Ga_{0.7}Sb$. These macrosteps are large enough to be observed by secondary electron scanning electron microscopy (SEM), as seen in Fig. 5(a). These macrosteps appear to be ~7-nm tall when measured via STM, with spacing between macrosteps on the order of 500–1000 nm.

B. Surface energy model

We postulate that it is the total surface area of the GaSb{110} surface that drives the formation of macrosteps on the surface. This driving force can be easily explained by a simple model which compares the surface energy of

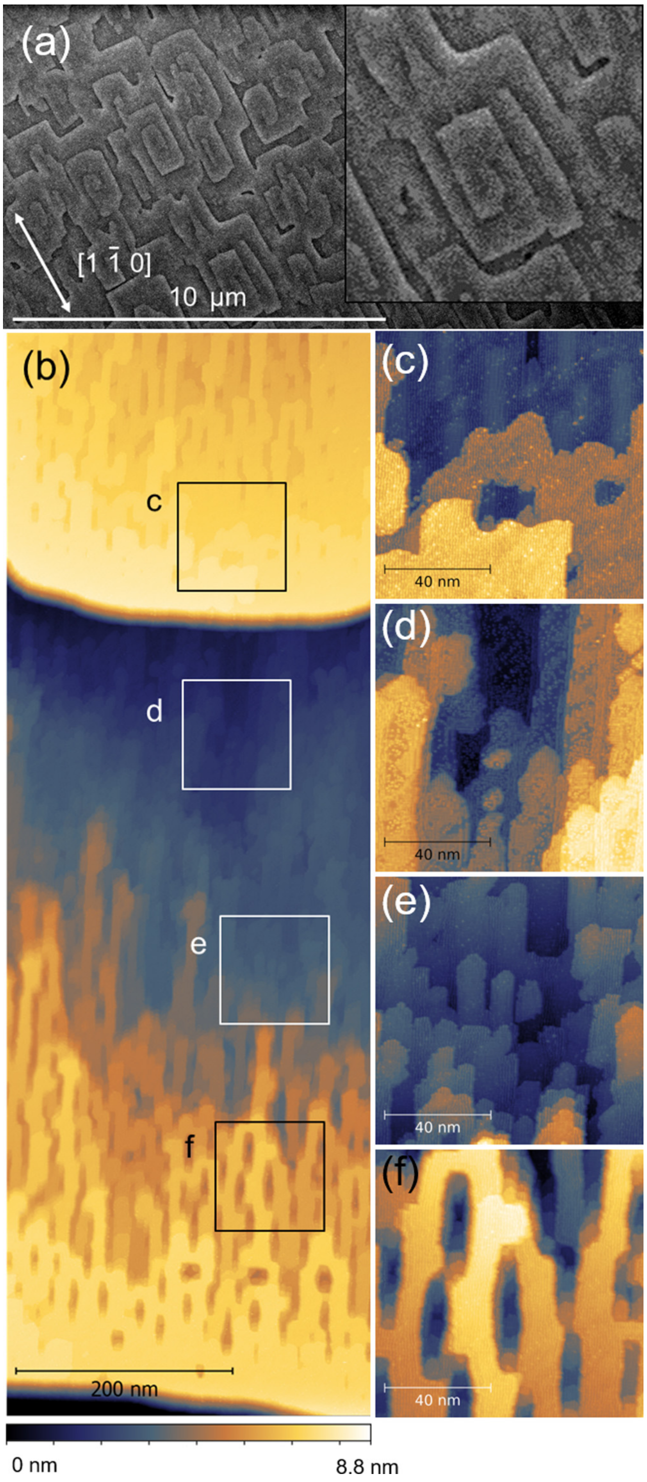

FIG. 5. (a) SEM of $\mathrm{Er_{0.3}Ga_{0.7}Sb}(001)$ surface, inset shows a blowup of a macrostep feature. (b) STM depicting a pair of macrosteps and the changing surface morphology across the terrace between them. Highlighted areas show positions of higher resolution images used to calculate ErSb surface coverage: (c) 14% ErSb, (d) 88% ErSb, (e) 70% ErSb, (f) 5% ErSb. Scale bar belongs to 4(b).

the out-of-plane and in-plane growth modes. GaSb in the out-of-plane, or vertical nanowire (VNW), growth regime is located around nanoparticles creating a porous structure with GaSb{110} sidewalls and horizontal nanowires. During in-plane, or horizontal nanowire (HNW), growth this excess GaSb which previously formed the pits around the nanoparticles is condensed into a large rectangular macrostep on the surface. A schematic of these two surface morphologies is shown in Fig. 6(a).

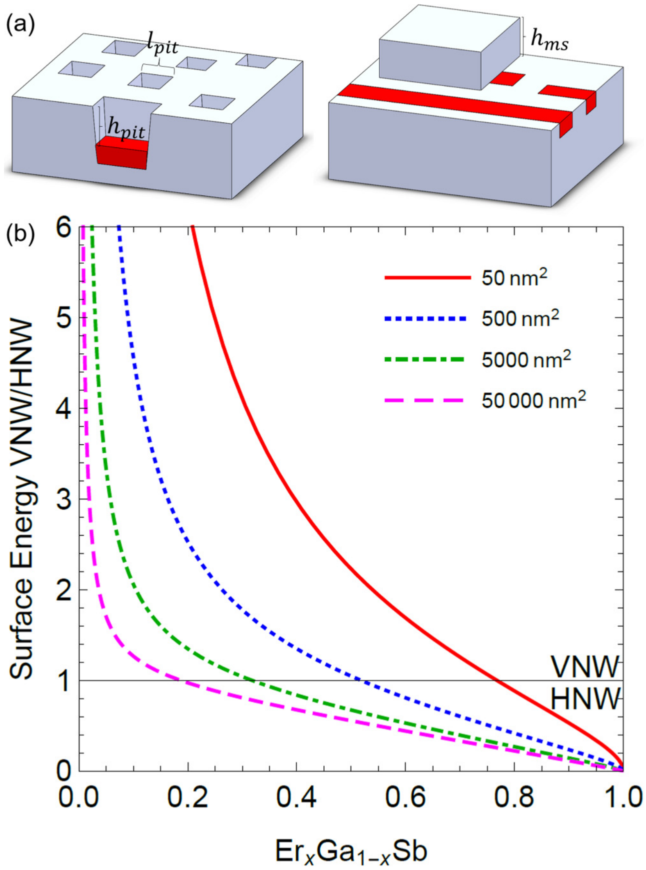

FIG. 6. (a) Diagram showing the two surface configurations used in the model. The macrostep on the right is comprised of the GaSb above the nanoparticles (h_{pit}). (b) Plot of Eq. (2) showing the ratio of surface energies between vertical nanowire and horizontal nanowire morphologies. Lines depict different sized areas contributing to a single macrostep. The transition occurs at lower Er concentrations as surface area of a single macrostep increases.

The total surface energy of the epilayer is given by

$$E = \sum s_{\mathrm{GaSb}\{110\}}\gamma_{\mathrm{GaSb}\{110\}} + \sum s_{\mathrm{GaSb}(001)}\gamma_{\mathrm{GaSb}(001)} + \sum s_{\mathrm{ErSb}(001)}\gamma_{\mathrm{ErSb}(001)} + \sum s_{\frac{\mathrm{ErSb}}{\mathrm{GaSb}(001)}}\gamma_{\frac{\mathrm{ErSb}}{\mathrm{GaSb}(001)}}. \quad (1)$$

The $S_{\mathrm{GaSb}\{110\}}$, $S_{\mathrm{GaSb}\{001\}}$, $S_{\mathrm{ErSb}(001)}$, $S_{\mathrm{ErSb/GaSb}(001)}$, terms in Eq. (1) represent the surface areas of the GaSb{110}/vacuum, GaSb(001)/vacuum, ErSb(001)/vacuum surfaces and the buried GaSb(001)/ErSb(001) interface formed when a macrostep overgrows a nanowire. The $\gamma_{\mathrm{GaSb}\{110\}}$, $\gamma_{\mathrm{GaSb}(001)}$, $\gamma_{\mathrm{ErSb}(001)}$, $\gamma_{\mathrm{ErSb/GaSb}(001)}$, terms represent the surface energies of the GaSb{110}/vacuum, GaSb(001)/vacuum, ErSb(001)/vacuum surfaces and the buried GaSb(001)/ErSb(001) interface. The buried interfaces between the ErSb nanowires and GaSb matrix not explicitly shown in Eq. (1) are assumed to have equivalent surface areas in both horizontal and vertical nanowire morphologies, this is true if the shape of a nanowire is the same in each case. In this model it is assumed that the surface area coverage of GaSb(001) and ErSb(001) is unchanged directly before and after the transition occurs, and that when calculating ΔE, the difference between the total surface energy of the in-plane nanowires ($E_{\parallel}$) and the total surface energy of the vertical nanowires ($E_{\perp}$) cancel resulting in

$$\begin{aligned}\Delta E &= E_{\parallel} - E_{\perp}\\ &= \sum s_{\mathrm{GaSb}\{110\}}\gamma_{\mathrm{GaSb}\{110\}} + \sum s_{\frac{\mathrm{ErSb}}{\mathrm{GaSb}\{001\}}}\gamma_{\frac{\mathrm{ErSb}}{\mathrm{GaSb}\{001\}}}\\ &\quad - \sum s'_{\mathrm{GaSb}\{110\}}\gamma_{\mathrm{GaSb}\{110\}},\end{aligned} \tag{2}$$

where the $S_{\mathrm{GaSb}\{110\}}$ and $S_{\mathrm{ErSb/GaSb}\{001\}}$ terms represent the in-plane nanowire growth surface and the $S'_{\mathrm{GaSb}\{110\}}$ represents the out-of-plane growth surface. The transition between surfaces occurs when $\Delta E = 0$, which results in the ratio

$$\frac{E_{\parallel}}{E_{\perp}} = 1 = \frac{\sum s_{\mathrm{GaSb}\{110\}}\gamma_{\mathrm{GaSb}\{110\}} + \sum s_{\frac{\mathrm{ErSb}}{\mathrm{GaSb}\{001\}}}\gamma_{\frac{\mathrm{ErSb}}{\mathrm{GaSb}\{001\}}}}{\sum s'_{\mathrm{GaSb}\{110\}}\gamma_{\mathrm{GaSb}\{110\}}}. \tag{3}$$

Substituting for particle and macrostep dimensions, assuming square-based pits around vertical nanowires and square macrostep features, results in the expression

$$\begin{aligned}\frac{E_{\parallel}}{E_{\perp}} &= C_1\frac{\sqrt{(1-x)}}{x} + C_2(1-x),\\ C_1 &= \frac{h_{\mathrm{ms}} l_{\mathrm{pit}}\sqrt{\frac{A h_{\mathrm{pit}}}{h_{\mathrm{ms}}}}}{h_{\mathrm{pit}} A}, \quad C_2 = \frac{\gamma_{\mathrm{GaSb/ErSb}}}{\gamma_{\mathrm{GaSb}\{110\}}}\frac{l_{\mathrm{pit}}}{4h_{\mathrm{ms}}},\end{aligned} \tag{4}$$

where h_{ms} is the height of the macrostep, l_{pit} and h_{pit} are the base length and height of a vertical nanowire pit, x is the Er content where $x = 1$ is pure ErSb and A is the total surface area contributing to macrostep formation. This model is plotted in Fig. 6(b), with values of $h_{\mathrm{ms}} = 7\,\mathrm{nm}$, $l_{\mathrm{pit}} = 4\,\mathrm{nm}$, and $h_{\mathrm{pit}} = 1.5\,\mathrm{nm}$ as estimated from STM measurements. The surface energy component of C_2 is unknown, but different values merely shift the position of the HNW/VNW crossover without impacting the overall shape of the plot. A value of $\frac{\gamma_{\mathrm{GaSb/ErSb}}}{\gamma_{\mathrm{GaSb}\{110\}}} = 8$ was used to provide a crossover similar to what is observed experimentally. A represents the area of the surface contributing GaSb to a single macrostep and should vary based on the temperature-dependent diffusion length of Ga on the surface. Several different values of A can be seen plotted in Fig. 6, all of which show that there is a critical threshold of Er composition when in-plane nanowires and formation of macrosteps results in lower total surface energy. The model predicts that the Er content required to reach the critical threshold for macrostep formation will monotonically decrease as substrate growth temperature increases. This model provides a clear driving force for macrostep formation motivated from the better surface to volume ratio achieved for GaSb{110} surfaces at higher Er concentrations.

C. Macrostep structure and evolution

Figure 5(b) shows an STM topography image along a terrace and across a macrostep. By using the same STS analysis of surface reconstructions shown in Fig. 4 the coverage of ErSb can be calculated at various points surrounding a macrostep. Areas near the bottom of a macrostep [Fig. 5(d)] exhibit very large concentrations of ErSb (88%), while areas near the top edge of a macrostep [Fig. 5(c)] show a much lower ErSb surface coverage (14%). As distance from the base of macrostep increases ErSb coverage drops with measured values of 70% at Fig. 5(e), and 5% at Fig. 5(f). Substantial diffusion of either Er or Ga on the terrace surface is required to explain this discrepancy. This agrees with previous results of ErSb growth on GaSb that report an Er-Ga exchange reaction and step-flow growth [28]. In the exchange reaction Er is observed to kick out Ga atoms that then diffuse across the surface to grow GaSb at step edges [28]. At greater Er compositions surface energy is minimized if Ga atoms diffuse to a macrostep and deposit there. This results in the equivalent of step-flow growth on a macrostep scale. This process also explains the difference in Er coverage between the top and base of a macrostep. The top of the macrostep is new GaSb growth that has not been exposed to Er deposition for very long, the base of a macrostep has had the longest exposure period and thus the most ErSb coverage.

The high ErSb surface coverage at the base of macrosteps will also favor macrostep growth. During step-flow growth diffusion rates are high enough that no attachment in the center of terraces occurs, Ga adatoms diffuse all the way to a step edge where bonding is more favorable before attaching to the surface. This step-flow growth mode can be characterized by the probability of an adatom attaching to an upstep versus a downstep [34]. When the upstep is more favored terrace growth is driven towards equally spaced terraces and is the growth mode seen in step flow growth of pure GaSb [34]. However, if the down step is favored, large terraces outgrow smaller terraces and step bunching occurs resulting in macrosteps [34].

Some GaSb deposition is observed on the terrace surface near the top of a macrostep. In this region Er concentration is low enough to fall within the out-of-plane growth regime and GaSb growth around nanoparticles does not have the large surface energy penalty associated with higher Er compositions. Growth backwards from the edge is also encouraged due to an Ehrlich-Schwoebel barrier at the step edge [35]. Figure 7 shows the proposed diffusion and growth of Ga adatoms on the surface as well as a ball-and-stick model of the unfavorable atomic bonding that would occur as a GaSb step overgrows an ErSb nanoparticle [36,37].

Cross-sectional high angle annular dark field scanning transmission electron microscopy (HAADF-STEM) was performed on an additional $\mathrm{Er_{0.3}Ga_{0.7}Sb}$ sample, see Fig. 8, grown under identical conditions as the sample shown in Fig. 5. The sample was prepared using a focused ion beam to cut and thin the cross section. This sample had ~25 nm of amorphous AlO_x deposited *in situ* via e-beam evaporation to preserve macrostep features on the surface. Figures 8(a) and 8(c) show a macrostep looking along the [110] and $[1\bar{1}0]$ zone axes, respectively. When viewed along these directions the zinc-blende crystal has a higher projected areal atomic density, which, in combination with the higher average atomic number (Z) of ErSb, makes the nanoparticles easily distinguishable as the brighter areas due to the Z contrast of HAADF-STEM. Macrosteps oriented along the [110] and $[1\bar{1}0]$ directions both show a predominantly uninterrupted

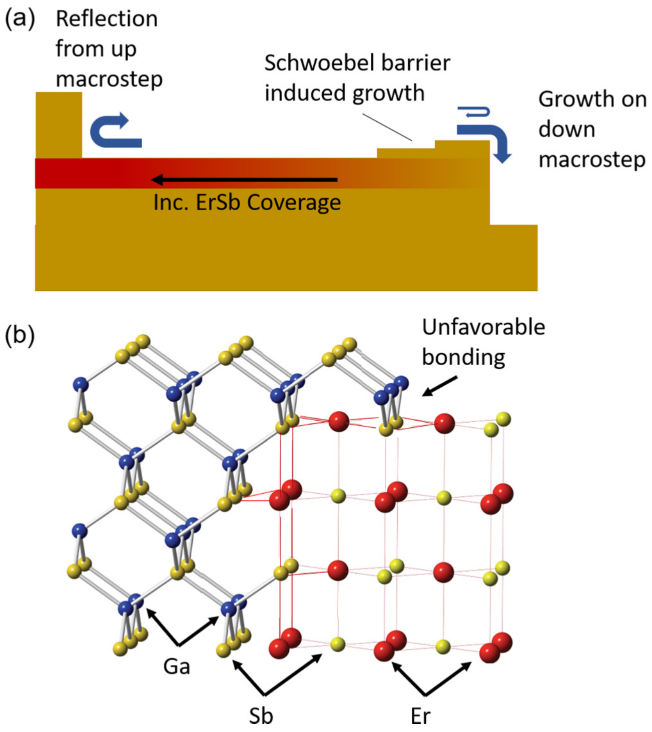

FIG. 7. (a) Diagram showing the growth model for Ga adatoms diffusing along the surface. Ga adatoms reflect from the bottom of a macrostep and most of the growth occurs from the top edge of a macrostep, while some growth occurs on the leading terrace of the macrostep due to the Schwoebel barrier. (b) Ball-and-stick model showing overgrowth of an ErSb nanoparticle by GaSb.

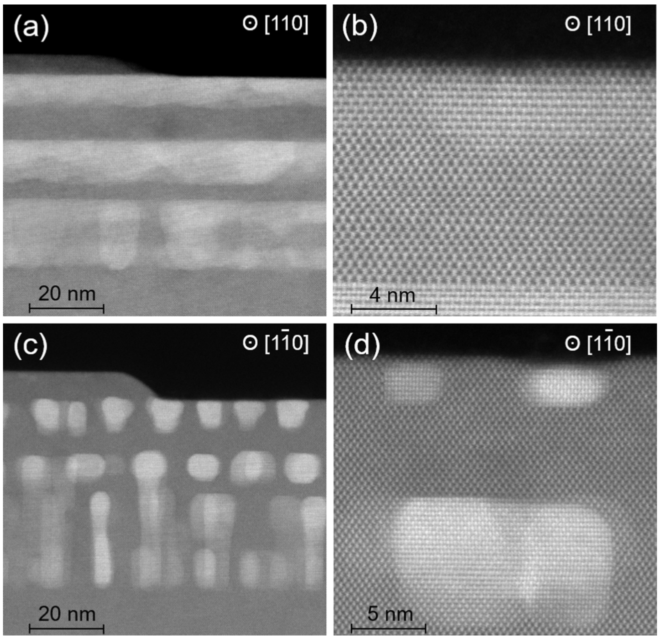

FIG. 8. HAADF-STEM of $Er_{0.3}Ga_{0.7}Sb$ samples capped with amorphous AlO_x. Lighter regions correspond to ErSb nanowires. (a) Image along the [110] direction perpendicular to the long axis of the nanowires. (b) First observable nanoparticles on the surface of the macrostep in (a) ~100 nm from the macrostep edge. (c) Image along the [1$\bar{1}$0] direction parallel long axis of nanowires. (d) First observable nanoparticles on the macrostep seen in (c) ~15 nm from step edge.

nanowire containing layer underneath them, this is further evidence that macrosteps grow in a step-flow fashion across the surface. A stationary macrostep should coincide with a discontinuity in the underlying nanowire layers. The spacing between subsequent nanowire layers is observed to match the height of the macrosteps.

Figures 8(b) and 8(d) show the first observable nanoparticle on top of the macrostep. For the [1$\bar{1}$0] facing macrostep [Fig. 8(a)] the ErSb is 100 nm from the step edge while the [110] facing macrostep [Fig. 8(b)] shows nanoparticles within 15 nm of the step edge. This discrepancy in macrostep growth is attributed to asymmetric diffusion rates along the GaSb(001) surface reconstruction [29,33] and is in agreement with the observed asymmetry in the nanowires and macrosteps observed in Fig. 5.

Overgrowth of GaAs on planar ErAs layers has been shown to result in nucleation of twinned GaAs islands [38]. To rule out the possibility of a defect generating macrosteps a 25-nm-thick $Er_{0.3}Ga_{0.7}Sb$ sample was grown without an AlO_x capping layer for characterization by electron channeling contrast imaging (ECCI). ECCI is sensitive to atomic displacements in a crystal such as the displacement from strain fields in dislocations and should reveal the presence of any strain inducing defects that might drive macrostep nucleation. Channeling conditions were found from the observed electron channeling pattern using a working distance of 5.3 mm and a beam current of 0.4 nA [39]. A few misfit dislocations were observed, Fig. 9 shows an ECCI image of the surface of an $Er_{0.3}Ga_{0.7}Sb$ film including a dislocation. However, the density of observed defects is much less than that of the macrosteps, from this we conclude that macrostep formation is not driven by defects that possess a strain field or change in crystal structure.

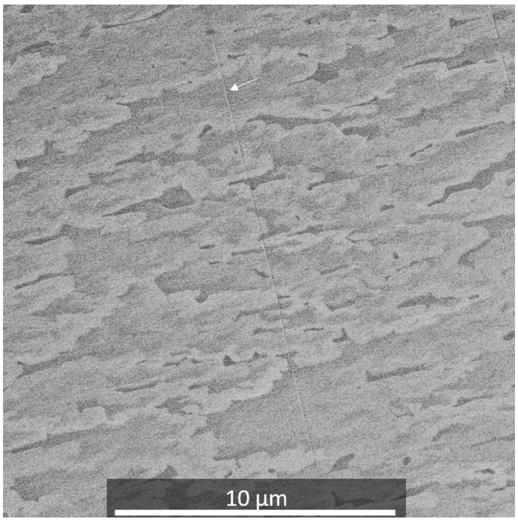

FIG. 9. ECCI image of a 25 nm $Er_{0.3}Ga_{0.7}Sb$ film grown on a GaSb(001) substrate. The only defects with observable strain fields in the sample are misfit dislocations, as seen in the center of the image. No defects are observed systematically under macrosteps.

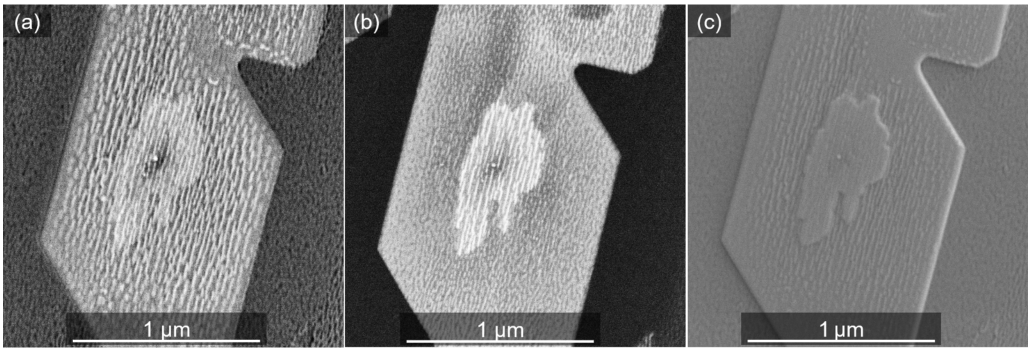

FIG. 10. A macrostep on a 25 nm $Er_{0.3}Ga_{0.7}Sb(001)$ surface imaged in three different modes, (a) ECCI showing surface ErSb nanowire distribution. (b) Backscatter electron image tilted 2.5° out of the channeling condition used for (a), nanowires from layers beneath the surface are now equally observed. (c) Secondary electron image showing surface features of the macrostep.

One benefit of the ECCI measurement is that the backscattered electrons in the measurement clearly show the high Z ErSb nanowires. Figure 10 shows SEM images taken in the ECCI channeling conditions, backscatter mode, and secondary electron mode. Since ErSb has a very similar crystal structure to GaSb many of the channeling conditions work for both phases. As a result, the ECCI image only shows ErSb nanowires directly on the surface where incident electrons behave as they would in a normal backscatter image. Deeper nanowires are invisible due to the presence of the channeling effect of the atomic lattice. In contrast the backscatter image shows all nanowires throughout the 25-nm-thick layer. The secondary electron image primarily shows the surface morphology of the macrostep. The ECCI image in Fig. 10(a) clearly shows that the surface nanowires near areas of recent growth such as the macrostep edge and the notch feature in the top right are smaller and less dense corroborating the conclusion from STM and TEM that macrostep flow occurs during growth, and nanowire coverage is a function of Er flux exposure time.

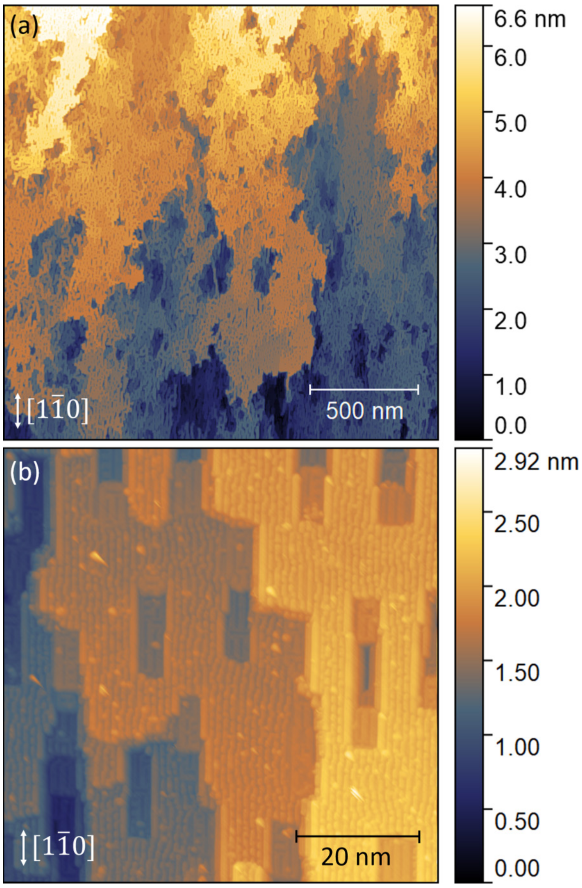

FIG. 11. (a) STM of 7.5 nm of $Er_{0.3}Ga_{0.7}Sb(001)$ surface, the beginning of step bunching can be seen. (b) shows ErSb nanoparticles are present one monolayer below the growth plane.

Figure 11 shows STM topography images of a 7.5-nm-thick $Er_{0.3}Ga_{0.7}Sb$ sample. This thickness should correspond to the start of in-plane nanowire growth observed in Fig. 8. Observed step bunching may indicate the beginning of macrostep formation. Simultaneously, ErSb particles are observed just one monolayer below the growth surface, instead of recessed in pits, these transitions agree with the proposed growth mechanisms.

IV. PROPOSED GROWTH MECHANISM

From these results it is possible to propose the requirements for in-plane nanowire formation:

(1) A surface energy difference between constituents such that overgrowth of nanoparticles by the matrix material is unfavorable.

(2) Step-flow growth conditions allowing macrosteps to grow across the surface.

(3) A reason for elongation of nanoparticles along a specific crystal direction, here assumed to be due to asymmetric surface diffusion of Er.

All three of these requirements must be met simultaneously to explain the observed phenomenon. Previous work proposed the importance of asymmetric surface diffusion but did not explain why the horizontal nanowires grow in strata with layers alternating with pure GaSb [28]. It is only once the other two requirements are met, resulting in macrosteps that grow via step flow across the surface, that the full structure observed for in-plane nanowires is explained.

Most of the other RE-V/III-V material systems should be capable of meeting the three criteria for in-plane nanowire growth. Of note are LuAs/GaAs and NdP/InP as potential candidates, both pairs of materials are nearly lattice matched to each other similar to ErSb/GaSb [11]. Nonlattice matched pairings are also of interest. The role of strain in the growth mechanism explored here has been ignored due to the close lattice matching of ErSb and GaSb. It is unknown if low strain is a requirement for in-plane nanowire growth. Some initial growths of ErAs/GaAs by the authors (results not shown) found it challenging to reproduce the high Group V surface diffusivities observed in ErSb/GaSb and resulted in very rough surfaces. Other growth techniques, such as metal organic chemical vapor deposition (MOCVD), which can reach higher substrate temperatures, may prove beneficial in achieving the requirement for high adatom surface diffusion of the matrix material.

Structures remarkably similar to the stratified nanowires observed here have been reported when attempting to grow Si with high C content [40–42]. Layers of nanoparticles have been observed separated by Si layers that are nanoparticle free [41]. The formation of these layered structures is found to be dependent on growth temperature, only occurring at elevated growth temperatures corresponding to high Si surface diffusivity [40]. These results seem to correlate to the behavior observed in macrostep formation for ErSb/GaSb. However, the Si(001) surface reconstruction rotates 90° each monolayer, so the growth of nanowires due to asymmetric surface diffusion is not expected to occur. The similarities between the Si/C layer structure and the ErSb/GaSb structures suggest that in-plane nanowire growth may be observed in material systems outside of the RE-V/III-V pairings, provided the additional requirement of anisotropic surface diffusion or another reason for anisotropic growth is met.

In conclusion we show that the transition from out-of-plane to in-plane nanowires in the ErSb/GaSb system is the result of a growth mode brought about by a change in surface morphology, characterized by the presence of large macrosteps and step-flow growth. The increase in ErSb coverage results in the GaSb matrix material forming macrosteps to reduce overall surface energy. The step-flow growth conditions allow for macrosteps to grow across the surface creating a layer of pure GaSb between layers of nanowires. Knowledge of this macrostep mediated growth mode implies that care must be taken when integrating horizontal nanowires into device heterostructures especially near sensitive layers as the macrosteps introduce a degree of surface roughness. The underlying mechanism for formation of horizontal nanowires observed here is potentially applicable to other pairs of materials with similar diffusion and surface energy properties.

ACKNOWLEDGMENT

This work was funded by the National Science Foundation (NSF) Grant No. DMR-1507875, we also acknowledge the use of facilities within the NSF Materials Research and Science and Engineering Center Grant No. (DMR 11–21053) at the University of California, Santa Barbara.

---

[1] D. Jung, J. Faucher, S. Mukherjee, A. Akey, D. J. Ironside, M. Cabral, X. Sang, J. Lebeau, S. R. Bank, T. Buonassisi, O. Moutanabbir, and M. L. Lee, Nat. Commun. **8**, 14204 (2017).

[2] J. Hemberger, A. Krimmel, T. Kurz, H.-A. Krug von Nidda, V. Y. Ivanov, A. A. Mukhin, A. M. Balbashov, and A. Loidl, Phys. Rev. B **66**, 094410 (2002).

[3] H. Lu, P. G. Burke, A. C. Gossard, G. Zeng, A. T. Ramu, J. H. Bahk, and J. E. Bowers, Adv. Mater. **23**, 2377 (2011).

[4] H. Lu, D. G. Ouellette, S. Preu, J. D. Watts, B. Zaks, P. G. Burke, M. S. Sherwin, and A. C. Gossard, Nano Lett. **14**, 1107 (2014).

[5] D. Leonard, M. Krishnamurthy, C. M. Reaves, S. P. Denbaars, and P. M. Petroff, Appl. Phys. Lett. **63**, 3203 (1993).

[6] J. W. Cahn, Acta Metall. **9**, 795 (1961).

[7] F. Léonard and R. C. Desai, Phys. Rev. B **57**, 4805 (1998).

[8] F. Léonard, M. Laradji, and R. C. Desai, Phys. Rev. B **55**, 1887 (1997).

[9] C. J. Palmstrøm, N. Tabatabaie, and S. J. Allen, Appl. Phys. Lett. **53**, 2608 (1988).

[10] D. C. Driscoll, M. P. Hanson, E. Mueller, and A. C. Gossard, J. Cryst. Growth **251**, 243 (2003).

[11] A. Guivarc'h, A. Le Corre, P. Auvray, B. Guenais, J. Caulet, Y. Ballini, R. Gúcrin, S. Députier, M. C. Le Clanche, G. Jézéquel, B. Lépine, A. Quémerais, and D. Sébilleau, J. Mater. Res. **10**, 1942 (1995).

[12] E. M. Krivoy, H. P. Nair, A. M. Crook, S. Rahimi, S. J. Maddox, R. Salas, D. A. Ferrer, V. D. Dasika, D. Akinwande, and S. R. Bank, Appl. Phys. Lett. **101**, 141910 (2012).

[13] A. G. Petukhov, W. R. L. Lambrecht, and B. Segall, Phys. Rev. B **50**, 7800 (1994).

[14] W. R. L. Lambrecht, B. Segall, A. G. Petukhov, R. Bogaerts, and F. Herlach, Phys. Rev. B **55**, 9239 (1997).

[15] C. Kadow, J. A. Johnson, K. Kolstad, J. P. Ibbetson, and A. C. Gossard, J. Vac. Sci. Technol. B **18**, 2197 (2000).

[16] C. C. Bomberger, M. R. Lewis, L. R. Vanderhoef, M. F. Doty, and J. M. O. Zide, J. Vac. Sci. Technol. B **35**, 030801 (2017).

[17] B. E. Tew, M. R. Lewis, C. Hsu, C. Ni, and J. M. O. Zide, J. Cryst. Growth **518**, 34 (2019).

[18] R. Salas, S. Guchhait, K. M. McNicholas, S. D. Sifferman, V. D. Dasika, D. Jung, E. M. Krivoy, M. L. Lee, and S. R. Bank, Appl. Phys. Lett. **108**, 182102 (2016).

[19] R. Salas, S. Guchhait, S. D. Sifferman, K. M. McNicholas, V. D. Dasika, D. Jung, E. M. Krivoy, M. L. Lee, and S. R. Bank, APL Mater. **5**, 96106 (2017).

[20] C. Kadow, A. W. Jackson, A. C. Gossard, J. E. Bowers, S. Matsuura, and G. A. Blake, Physica E **7**, 97 (2000).

[21] H. P. Nair, A. M. Crook, and S. R. Bank, Appl. Phys. Lett. **96**, 222104 (2010).

[22] R. Koltun, J. L. Hall, T. E. Mates, J. E. Bowers, B. D. Schultz, and C. J. Palmstrøm, J. Vac. Sci. Technol. B **31**, 41401 (2013).

[23] Y. Zhang, K. G. Eyink, L. Grazulis, M. Hill, J. Peoples, and K. Mahalingam, J. Cryst. Growth **477**, 19 (2017).

[24] C. C. Bomberger, L. R. Vanderhoef, A. Rahman, D. Shah, D. B. Chase, A. J. Taylor, A. K. Azad, M. F. Doty, and J. M. O. Zide, Appl. Phys. Lett. **107**, 102103 (2015).

[25] P. Dongmo, M. Hartshorne, T. Cristiani, M. L. Jablonski, C. Bomberger, D. Isheim, D. N. Seidman, M. L. Taheri, and J. Zide, Small **10**, 4920 (2014).

[26] P. F. Miceli, C. J. Palmstrøm, and K. W. Moyers, Appl. Phys. Lett. **58**, 1602 (1991).

[27] A. J. Young, B. D. Schultz, and C. J. Palmstrøm, Appl. Phys. Lett. **104**, 73114 (2014).

[28] J. K. Kawasaki, B. D. Schultz, H. Lu, A. C. Gossard, and C. J. Palmstrøm, Nano Lett. **13**, 2895 (2013).

[29] B. D. Schultz, S. G. Choi, and C. J. Palmstrøm, Appl. Phys. Lett. **88**, 243117 (2006).

[30] B. D. Schultz and C. J. Palmstrøm, Phys. Rev. B **73**, 241407(R) (2006).

[31] S. Chalmers, H. Kroemer, and A. Gossard, Appl. Phys. Lett. **57**, 1751 (1990).

[32] R. M. Feenstra, Phys. Rev. B **50**, 4561 (1994).

[33] E. Penev, S. Stojković, P. Kratzer, and M. Scheffler, Phys. Rev. B **69**, 115335 (2004).

[34] J. Y. Tsao, *Materials Fundamentals of Molecular Beam Epitaxy* (Academic Press, San Diego, 1993).

[35] R. L. Schwoebel and E. J. Shipsey, J. Appl. Phys. **37**, 3682 (1966).

[36] P. F. Miceli and C. J. Palmstrøm, Phys. Rev. B **51**, 5506 (1995).

[37] K. Momma and F. Izumi, J. Appl. Cryst. **44**, 1272 (2011).

[38] T. Sands, C. J. Palmstrøm, J. P. Harbison, V. G. Keramidas, N. Tabatabaie, T. L. Cheeks, R. Ramesh, and Y. Silberberg, Mater. Sci. Rep. **5**, 99 (1990).

[39] J. I. Dietz, S. D. Carnevale, S. A. Ringel, D. W. McComb, and T. J. Grassman, J. Vis. Exp. **101**, e52745 (2015).

[40] H. J. Osten, E. Bugiel, and P. Zaumseil, J. Appl. Phys. **82**, 231 (1997).

[41] E. T. Croke, F. Grosse, J. J. Vajo, M. F. Gyure, M. Floyd, and D. J. Smith, Appl. Phys. Lett. **77**, 1310 (2000).

[42] J. Vollmer, J. Hegedüs, F. Grosse, and J. Krug, New J. Phys. **10**, 053017 (2008).